

**ENERGETICS OF BIPOLAR MOLECULAR  
OUTFLOWS  
IN STAR FORMATION REGIONS**

APPROVED:

Supervisor: \_\_\_\_\_

\_\_\_\_\_

\_\_\_\_\_

**ENERGETICS OF BIPOLAR MOLECULAR  
OUTFLOWS  
IN STAR FORMATION REGIONS**

by

**SOOJONG PAK, B.S.**

**THESIS**

Presented to the Faculty of the Graduate School of  
The University of Texas at Austin  
in Partial Fulfillment  
of the Requirements  
for the Degree of

**MASTER OF ARTS**

THE UNIVERSITY OF TEXAS AT AUSTIN

May, 1994

TO MY PARENTS, PARENTS-IN-LAW,  
AND MY WIFE

## Acknowledgments

I would like to thank my advisor, Prof. Jaffe, for his guidance and encouragement. My gratitude goes as much to Prof. Evans for his guidance when Prof. Jaffe was in Germany, and to Prof. Lacy for his very helpful comments. I would also like to thank Mike Luhman and Luke Keller in our FPS lab for their patient and friendly relationship with me, and Minho Choi for his introducing me to the science of outflows and his guide to computer. I recall that Jai Chan Hwang, Hye-rim Noh, Insu Yi, and Soon-wook Kim helped me a lot during my first year in Austin. Finally, I thank my elder brother, Soo-Keun Pak, my elder sister, Suehee Pak, and their families.

SOOJONG PAK

*The University of Texas at Austin*

*May, 1994*

# ABSTRACT

## ENERGETICS OF BIPOLAR MOLECULAR OUTFLOWS IN STAR FORMATION REGIONS

by

SOOJONG PAK, B.S.

SUPERVISING PROFESSOR: DANIEL T. JAFFE

We built a new near-infrared Fabry-Perot spectrometer (UT FPS) that is optimized with a large beam for surface brightness measurements. With this instrument, we observed the  $\text{H}_2$   $v = 1 \rightarrow 0$   $S(1)$  ( $\lambda = 2.122\mu\text{m}$ ) transition line from shocked regions in bipolar molecular outflows. We extrapolate from the flux of this line to the total cooling energy and compare the observed radiation energy with the kinetic energy of the swept-up gas. We estimate how efficiently the stellar wind transfers its kinetic energy to the ambient cloud, comparing the  $\text{H}_2$  luminosity with the kinetic energy inferred from a momentum conserving outflow model and an energy conserving model.

## Table of Contents

Acknowledgments	iv
<b>ABSTRACT</b>	<b>v</b>
Table of Contents	vi
<b>1. INTRODUCTION</b>	<b>1</b>
<b>2. INSTRUMENTATION</b>	<b>6</b>
2.1 Why Do We Need A New Spectrometer ? . . . . .	6
2.2 Noise . . . . .	7
2.3 Fabry–Perot Interferometer . . . . .	10
2.4 University of Texas Fabry–Perot Spectrometer . . . . .	13
2.5 Shortcomings of Fabry–Perot . . . . .	16
2.6 High Voltage Amplifier . . . . .	17
2.7 Automatic Alignment Program . . . . .	19
<b>3. OBSERVATIONS</b>	<b>22</b>
<b>4. RESULTS</b>	<b>24</b>
4.1 Cepheus A . . . . .	24
4.2 L1448 . . . . .	28
4.3 Evidence for Diffuse Emission in L1551 . . . . .	30
4.4 Shocked H <sub>2</sub> Luminosity . . . . .	31

4.5	Shocked Total Luminosity . . . . .	35
<b>5.</b>	<b>DISCUSSION</b>	<b>37</b>
5.1	Stellar Wind as Outflow Source . . . . .	37
5.2	Energy Conserving Model and Momentum Conserving Model . .	38
5.3	Comparing the Models with the Observation . . . . .	42
<b>6.</b>	<b>CONCLUSIONS</b>	<b>45</b>
	<b>BIBLIOGRAPHY</b>	<b>47</b>
	Vita	

## Chapter 1

### INTRODUCTION

The fundamental idea of star formation theory is that an interstellar molecular cloud collapses by its own gravitational force. If only thermal pressure supports the cloud against the gravitational force, the Jeans mass ( $M_J$ ) determines the minimum cloud mass which is dynamically unstable,

$$M_J = \left( \frac{\pi kT}{\mu m_H G} \right)^{\frac{3}{2}} \frac{1}{\rho^{\frac{1}{2}}} \approx 18 \frac{T^{\frac{3}{2}}}{n^{\frac{1}{2}}} M_{\odot}, \quad (1.1)$$

where  $T$  is the temperature [K] and  $n$  the total number of particles per  $\text{cm}^3$ . The collapse of the molecular cloud is initially isothermal, because heavy molecules and grains are very effective coolants. We can estimate the collapse time scale from the free-fall time,

$$\tau_{ff} = \left( \frac{3\pi}{32G\rho} \right)^{\frac{1}{2}} \approx \frac{3.4 \times 10^7}{n^{\frac{1}{2}}} \text{ years}. \quad (1.2)$$

The Jeans mass analysis leads to the conclusion that almost all of the clouds are unstable to gravitational collapse. Also, given the short free-fall times for dense interstellar clouds, most molecular material should have formed into stars long ago.

The obvious resolution of this problem is that the thermal energy of the gas is not the only thing balancing the self-gravity. Rotation, magnetic fields, and turbulence are possible candidates to support the cloud. Both rotation and magnetic support, however, are direction-oriented forces which cannot

support the whole structure of the cloud. Turbulent pressure can be treated as an isotropic pressure analogous to the thermal pressure. The observed line width ( $\Delta v \sim 6 \text{ km s}^{-1}$ ) in some clouds implies strongly supersonic random motions. One problem with the turbulent support theory is that collisions between supersonic gas streams may dissipate the relative kinetic energy very efficiently by shock radiation. Scalo and Pumphrey (1982) numerically calculated the supersonic turbulent dissipation using N-body simulations of a system of interacting fragments. They concluded that the fragment motions do not decay so efficiently and turbulent support can persist without any external source of kinetic energy input for about 10 free-fall times.

Norman and Silk (1980) suggested that high-velocity winds from low-mass pre-main-sequence stars provide a continuous dynamic input into molecular clouds. Their idea is based on the clumpy cloud model, i.e., many small, dense, and cold clumps are immersed in a more diffuse interclump medium (ICM). The winds sweep out dense shells and make bubbles which intersect with other bubbles. New clumps form at the shell intersections and the ICM is replenished by the new clumps. The dynamics of the clumps controls further low-mass star formation. They assumed that this feedback process of star formation only applies to low-mass star formation, and massive star formation is stimulated by an external trigger, e.g., spiral density wave shocks or nearby supernova blast waves.

The idea of Norman and Silk was supported by the discovery of highly energetic bipolar molecular outflows from young stellar objects (YSOs) (Snell, Loren, and Plambeck 1980). During the past decade, molecular out-

flows have been extensively observed and studied. One of the implications of the study of molecular outflows is the existence of copious mass loss from the associated YSOs. It is generally accepted that during early stages of star formation, the forming star generates a very fast, well collimated bipolar wind ( $v_w \sim 300 \text{ km s}^{-1}$ ) that sweeps up the ambient gas in its vicinity (Bachiller and Gómez-González 1992). A part of the wind kinetic energy could replenish turbulence in the parental molecular cloud as Norman and Silk (1980) proposed.

Most of the observational work on molecular outflows has been performed with dipole transitions between low rotational levels of diatomic molecules, e.g., CO and CS, because these dipole transitions are easily excited at low temperature and the emission lines in the mm wavelength band are easily detectable with ground based telescopes. The morphology, dynamics, and the mass of the outflow can be derived from the mm observations. Bachiller and Gómez-González (1992) summarized the observational features of the flows. Most molecular outflows are *bipolar*; Doppler shifted (redshifted and blueshifted) lobes are spatially displaced on either side of the YSO. The *collimation* factor, i.e., the ratio of the outflow length to its width for each lobe, is in the range from 2 to 5. The measured flow sizes range from less than 0.1 pc to about 5 pc. The observed terminal velocities range from a few  $\text{km s}^{-1}$  to over  $100 \text{ km s}^{-1}$ , and the kinematical time-scale (outflow age), i.e., the flow length divided by the terminal velocity, ranges from a few  $10^3 \text{ yr}$  to about  $10^5 \text{ yr}$ . The total molecular mass of the outflowing material ranges from a few  $10^{-2} M_\odot$  to about  $10^2 M_\odot$ , which implies that the outflows consist of swept-up material instead of ejected material from the star.

The interaction of the high velocity ( $v_s \geq 10 \text{ km s}^{-1}$ ) molecular outflows with the surrounding ambient gas produces strong shock waves which compress, heat, and accelerate the ambient material. If the cooling time of the shocked gas is considerably shorter than the age of the outflow, the outflow is isothermal and the excess energy is radiated away. One of the most important theoretical questions about the outflow mechanism is whether the flows are driven in a momentum-conserving manner (McKee and Hollenbach 1987) or the energy in the driving wind is converted adiabatically into kinetic energy (a model of energy driven flows, Kwok and Volk 1985).

The radiation energy from the shocked region is in the form of spectral emission lines, because the regions are cooled by inelastic collisions. We are able to observe only a few emission lines from the shocked regions. In order to deduce the energy from the unobserved cooling lines, we are required to know the thermodynamic status of the shocked region or the magnetohydrodynamic (MHD) mechanism of the shock waves. Before 1980, studies of interstellar shock waves had assumed that the magnetic field is negligible ( $\rho_0 v_s^2 \gg B_0^2/8\pi$ ) or the magnetic field is frozen into the interstellar gas and amplified as the gas is compressed (McKee and Hollenbach 1980). The magnetic field, however, is coupled only to charged particles (ion-electron fluid) and the magnetized particles may not be coupled with the neutral particles to have the same velocity motions. When the charged fluid can propagate with magnetosonic waves ( $v_{Alfvén} = [B^2/4\pi\rho]^{1/2}$ ) at speeds greater than the shock speed ( $v_s$ ), the shock has a *magnetic precursor* (Draine 1980). In this case, the magnetic field can begin to be compressed and accelerated by the shock before the neutral-gas shock arrives, and the ion-electron flow variables ( $\rho_i$ ,  $T_i$ ,  $v_i$ ) are continuous at

the shock front.

Even with the magnetic precursor, if the magnetic field is not strong enough to couple the ion-electron fluid to the neutral fluid, the neutral flow variables ( $\rho_n$ ,  $T_n$ ,  $v_n$ ) are discontinuous at the shock front. We can use the Rankine-Hugoniot jump conditions for the neutrals, and this models a jump (*J-type*) shock. In the case that the magnetic field is strong enough to couple the ion-electron fluid to the neutral fluid, the neutral flow variables are continuous, and this is a continuous (*C-type*) shock. The density, the magnetic field, and ionization fraction in the preshock gas, and the velocity of the shock determine whether the shock is *J-type* or *C-type* (Hollenbach, Chernoff, and McKee 1989). It is very difficult, however, to know the physical conditions in the preshock gas and at the shock front.

In this project, we observe the shock-excited H<sub>2</sub> vibration-rotation line  $v = 1 \rightarrow 0 S(1)$  ( $\lambda = 2.122 \mu\text{m}$ ) in Cepheus A and L1448 and deduce the total shocked luminosity. The total radiation energy is compared with the kinetic energy in the swept-up ambient medium. We describe our new near-infrared spectrometer in Chapter 2, and our observations in Chapter 3. In Chapter 4, we extrapolate from the detected H<sub>2</sub> 2.122  $\mu\text{m}$  line luminosity to the total shocked luminosity by using the *C-type* shock model and the *J-type* shock model. The dynamical interaction of the wind with the ambient gas is discussed with the momentum conserving model and the energy conserving model in Chapter 5. Finally, we conclude our work and suggest future observations in Chapter 6.

## Chapter 2

### INSTRUMENTATION

#### 2.1 Why Do We Need A New Spectrometer ?

Models of MHD shocks in molecular gas imply that emission in the  $\text{H}_2$   $v = 1 \rightarrow 0$   $S(1)$  line should be appreciable for  $v_{shock} \geq 10 \text{ km s}^{-1}$  (see the review in Chapter 1). It should, in principle, be possible to infer the existence of shock-excited regions from observations of high-velocity CO emission. In Cepheus A and L1551, the high-velocity CO emission regions extend to  $10' \times 8'$  (Levreault 1985) and  $10' \times 30'$  (Moriarty-Schieven and Snell 1988) respectively.

To observe such faint and extended  $\text{H}_2$  emission sources, we require a near-infrared spectrometer that is optimized with a large beam for surface brightness measurements. The detector array camera on which most infrared astronomers are concentrating is not an optimal instrument for these kinds of objects, because the camera cannot cover the whole emission region in a limited observational time and cannot provide a way to reliably subtract nightsky and thermal background emission.

For the experiment described here, we use a Fabry-Perot interferometer and a photovoltaic indium antimonide (InSb) detector ( $\eta \sim 0.6$ ). The following description and calculations are based on the University of Texas Fabry-Perot Spectrometer System and the 2.7 m telescope at the McDonald Observatory.

## 2.2 Noise

Noise, signal fluctuations of a random nature, limits the sensitivity of a spectrometer. We can separate the noise sources into three types: photon noise, intrinsic detector noise, and read noise (Kitchin 1991).

The photon noise or signal noise arises from the quantum character of the incoming signal on the detector. The arrival rate of photons fluctuates and the detected number of photons can be characterized by a Poisson distribution. The photon noise in a given integration time is the square root of the average number of detected photons in that time. The electromagnetic sources of the signal are separated into the line emission from the astronomical objects and background thermal radiation, e.g., the atmosphere of the earth, the telescope, the spectrometer, etc. At the detector, the absorbed energies per second from the object ( $P_{obj}$ ) and from the background ( $P_{back}$ ) are,

$$P_{obj}[\text{erg s}^{-1}] = IA\Omega \tau_{obj}\eta \quad (2.1)$$

and

$$P_{back}[\text{erg s}^{-1}] = \varepsilon B_{\lambda}(T)\Delta\lambda A\Omega \tau_{back}\eta, \quad (2.2)$$

where  $I$  is the line intensity of the source whose spectral profile is close to the  $\delta(\lambda - \lambda_o)$  function,  $\varepsilon$  is the emissivity of the background radiation source,  $B_{\lambda}(T)$  is the Planck function,  $\Delta\lambda$  is the bandwidth accepted by the cryogenic part or spectrometric part of the system,  $A$  is the collecting area of the primary mirror,  $\Omega$  is the solid angle field of view of the telescope (assuming  $\Omega_{source} \gg \Omega$ ),  $\tau$  is the transmission of the optical components in the telescope and the spectrometer, and  $\eta$  is the quantum efficiency of the detector. The value of area–solid

angle product ( $A\Omega$ ) is conserved at the primary mirror of the telescope, at the spectrometer, and at the detector. For a typical intensity of the H<sub>2</sub> emission ( $P_{obj} \approx 10^{-9}$  erg s<sup>-1</sup>) and for that of background ( $P_{back} \approx 10^{-7}$  erg s<sup>-1</sup>), the dominant signal source is the background radiation, so that we call the photon noise *background noise*. The background noise in number of electrons ( $\eta$  times number of photons)

$$N_{back} = \left[ \frac{\lambda}{hc} P_{back} t \right]^{\frac{1}{2}}, \quad (2.3)$$

where  $t$  is the integration time.

The intrinsic noise originates inside the detector, and the photovoltaic detector has Johnson noise and dark-current shot noise. The *Johnson noise* or thermal noise is generated from the thermal motion of charge carriers in a resistor and depends only on the temperature ( $T \sim 50\text{K}$ ) and the resistance ( $R \sim 10^{12}\Omega$ ) of the detector itself,

$$N_{Johnson} = \frac{1}{e} \left[ \frac{4kT}{R} t \right]^{\frac{1}{2}}, \quad (2.4)$$

where  $e$  is the charge of an electron ( $1.6 \times 10^{-19}$  C). The random arrival rate of carriers at the  $p-n$  junction in the detector generates the *dark current shot noise* which is a function of the internal dark current ( $I_{dark}$ ),

$$N_{dark} = \left[ \frac{2I_{dark}}{e} t \right]^{\frac{1}{2}}. \quad (2.5)$$

The *read noise* ( $N_{read}$ ) arises from converting the generated charge at the detector into a readable form of voltage and amplifying that voltage. The detector itself has a capacitance and integrates the generated charge during one exposure time (0.1 – 2 sec). An integrating preamplifier converts the charge to

voltage and amplifies the voltage, and an analog–digital (A/D) converter reads a series of sample voltages at a rate of 10 KHz ( $B$ ) which is limited by the A/D bandwidth. We coded a routine to get the best slope of the integrated sample values with the least squares method (Chapman et al. 1990). The value of the slope corresponds to the detected signal. If we assume that read noise dominates over the other noise sources, we can calculate the read noise by multiplying the statistical slope error by the integration time,

$$N_{read} = N_{sample} \left[ \frac{12}{Bt} \right]^{\frac{1}{2}}, \quad (2.6)$$

where  $N_{sample}$  is the error (root mean square) of each sample.

The total noise is,

$$N_{total}^2 = N_{back}^2 + N_{dark}^2 + N_{Johnson}^2 + N_{read}^2. \quad (2.7)$$

For short integration times the read noise ( $\propto t^{-\frac{1}{2}}$ ) is dominant and for long integration times the background noise, dark current noise, and Johnson noise ( $\propto t^{\frac{1}{2}}$ ) become increasingly important. Assuming that the noise is a function of the integration time,  $N(t)$ , we can find the optimum integration time ( $t_{op}$ ), at which the total noise is minimum, by equating the read noise function (Equation 2.6) and the other noise functions (Equations 2.3, 2.4, and 2.5),

$$N_{read}^2 = N_{back}^2 + N_{dark}^2 + N_{Johnson}^2. \quad (2.8)$$

From the signal value in number of electrons,

$$S = \frac{\lambda}{hc} P_{obj} t, \quad (2.9)$$

the signal to noise ratio ( $S/N$ ) can be expressed as a function of the integration time,  $S/N \propto t^\alpha$ . The power of  $t$ ,  $\alpha$ , is  $3/2$  at  $t < t_{op}$  and  $1/2$  at  $t > t_{op}$ . In section 2.4, we present calculated values of each noise source.

### 2.3 Fabry–Perot Interferometer

We use a large surface area detector and a short focal length coupling lens, whose value of  $A\Omega$  is large enough to detect low surface brightness, extended sources. A *grating spectrometer*, however, is not appropriate for large  $A\Omega$  and small  $\Delta\lambda$ , because both of the values are proportional to the width of the slit ( $W$ ), i.e.,

$$A\Omega = \frac{\pi}{4}Wh \left(\frac{D}{f}\right)^2, \quad \Delta\lambda \simeq \lambda \frac{W}{d} \left(\frac{D}{f}\right), \quad (2.10)$$

where  $h$  is the height of the slit,  $d$  is the width of the grating, and  $D$  and  $f$  are the diameter and focal length of the telescope. For typical parameters of the grating and telescope, the spectral resolving power ( $\lambda/\Delta\lambda$ ) of 2000 corresponds to a several arc second beam size. With a Fabry–Perot interferometer or etalon (FP) we can maximize the beam size,  $\Omega$ , to square arcminutes, even though large  $A\Omega$  slightly reduces the spectral resolving power. The main disadvantage of the FP in observation is that we cannot get all channels in the line profile in one integration, but we have to scan across the line, increasing the total observation time.

The FP consists of two flat semi-transparent, parallel mirrors separated by some distance ( $l$ ). Light incident on the mirror surface will undergo multiple reflections between the mirrors. The different reflections interfere, resulting in a narrow bandwidth being transmitted and most of the radiation being reflected by the FP. When we fix the distance of the two mirrors, a series of wavelengths is transmitted in different orders of interference. The wavenumber (in units of  $\text{cm}^{-1}$ ) difference between adjacent transmission maxima is called

the free spectral range (FSR),

$$\Delta \left[ \frac{1}{\lambda} \right]_{FSR} = \frac{1}{2l}. \quad (2.11)$$

The finesse ( $F$ ), to which the resolvable spectral bandwidth is inversely proportional, is the effective number of interfering beams and the most important performance parameter of the FP. Mirror reflectivity ( $F_{ref}$ ), parallelism and planeness of the mirrors ( $F_{pp}$ ), and the range of the incident angles ( $F_{ang}$ ) contribute to individual finesse,

$$F_{ref} = \frac{\pi\sqrt{R}}{1-R}, \quad (2.12)$$

$$F_{pp} = \frac{\lambda}{2\Delta s}, \quad (2.13)$$

and

$$F_{ang} = \frac{\lambda}{l(\Delta\theta)^2}, \quad (2.14)$$

where  $R$  is the mirror reflectance,  $\Delta s$  is the deviation from parallelism and planeness, and  $\Delta\theta$  is the range of the incident angle to the FP plate ( $A\Omega = A_{FPplate}\pi(\Delta\theta)_{max}^2$ ). The net finesse can be estimated as,

$$F_{net}^{-2} \simeq F_{ref}^{-2} + F_{pp}^{-2} + F_{ang}^{-2}. \quad (2.15)$$

When we assume that only  $F_{ref}$  is effective, the formula of the instrument spectral profile is

$$I(\lambda, l, \theta) = \left(1 - \frac{\alpha}{1-R}\right)^2 \left[1 + \frac{4R}{(1-R)^2} \sin^2 \left(\frac{2\pi l \cos \theta}{\lambda}\right)\right]^{-1} \quad (2.16)$$

where  $\alpha$  is the absorbed or scattered energy fraction on coated surfaces, and  $\theta$  is incident angle (Born and Wolf 1965; Moore, David, and Coplan 1988). In Figure 2.1 we plot several profiles for various  $R$  with a point source ( $\theta = 0$ ) and  $\alpha = 0.004$ . A convolution of this instrument profile and an object emission profile will make an observed spectral line profile.

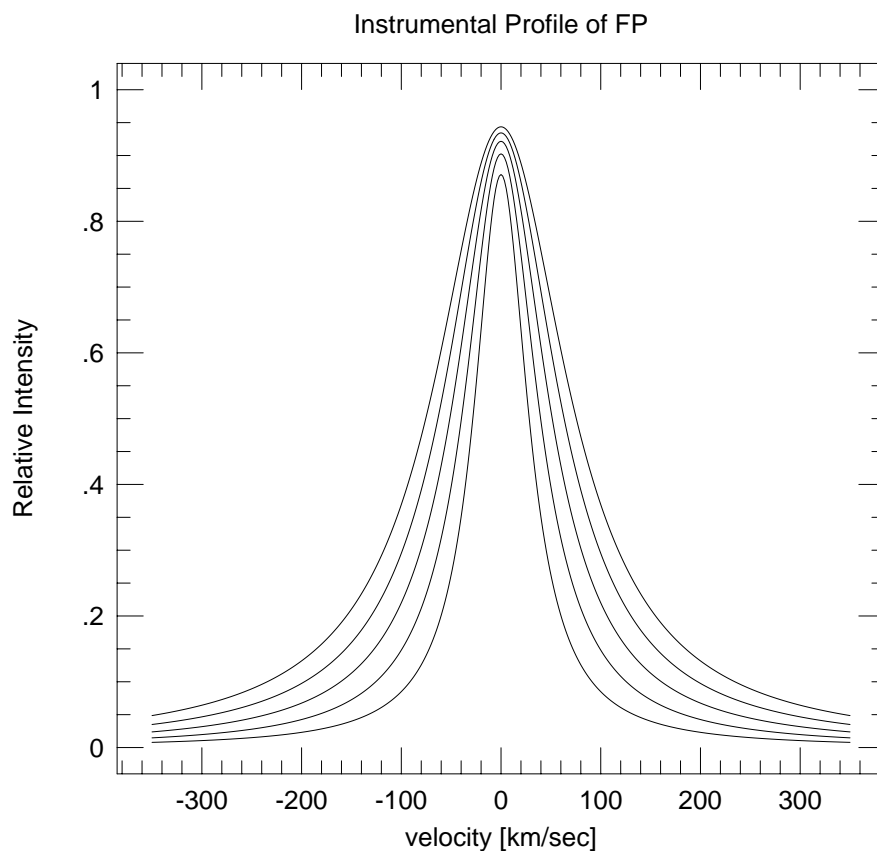


Figure 2.1.— Instrumental Profile of Fabry-Perot Spectrometer in velocity units with various reflectivities ( $R$ ). From the broadest profile to the narrowest profile,  $R$ 's are 0.86 ( $F_{ref} = 20.8$ ), 0.88 (24.6), 0.90 (29.8), 0.92 (37.7), and 0.94 (50.8). We assume that the source is point ( $\theta = 0$ ) and  $\alpha = 0.004$ . The free spectral range (FSR) is  $3,333 \text{ km s}^{-1}$ .

## 2.4 University of Texas Fabry–Perot Spectrometer

The University of Texas Fabry-Perot Spectrometer (UT FPS) is designed to maximize  $A\Omega$  and minimize noise. The optical layout is shown in Figure 2.2. First, the focused beam from the telescope (F/18 for the McDonald 2.7 m telescope) enters the fore-optics box. A 46 cm focal length paraboloidal mirror collimates the beam from the telescope and two flat mirrors reflect the collimated beam to the FP. The beam passes through a  $\text{CaF}_2$  window into a 48–55 K (solid nitrogen temperature) dewar. The 1 % fixed interference filter next to the window selects the 90th order of interference at  $2.12 \mu\text{m}$ . Finally the beam is focused by a 3.8 cm diameter and 3.42 cm focal length silicon meniscus lens and illuminates a  $1 \text{ mm}^2$  square InSb detector (COBE series, Cincinnati Inc.). The generated electrons on the detector are integrated by a low noise integrating amplifier (JF-4 model, Infrared Laboratories Inc.). The JF-4 consists of a hybrid circuit containing a balanced junction field-effect transistor (JFET) with a voltage gain of 0.8–0.9, and an input capacitance of 7.5 pF. The JFET needs an external reset pulse to remove the collected charge from the integrating gate before the exposure. A pre-amplifier (RS-1 model, Infrared Laboratories Inc.) amplifies the voltage signal from the JF-4 with gain of 100 and the PC based A/D converter (LSDAS-16, Analogic Co.) reads the final signal. In Table 2.1, we calculate the values of the various noise sources in this system for different integration times.

We use a Burleigh Inc. TL-38 Tunable Etalon in our spectrometer system. In this FP, two reflecting etalon plates are separated by  $l \simeq 100 \mu\text{m}$  and the reflectance ( $R$ ) of each plate surface is about 90 %. The etalon plates

Figure 2.2.— A schematic diagram of the optical system of Texas Fabry-Perot Spectrometer.

TABLE 2.1  
Individual Noise

CONTRIBUTOR	T[K]	$\Delta\lambda[\mu\text{m}]$	$\varepsilon$	N[e]
window	273	$2.44 \times 10^{-2}$	0.10	$254 t^{\frac{1}{2}}$
Fabry-Perot	278	$2.44 \times 10^{-2}$	0.10	$350 t^{\frac{1}{2}}$
fore-optics box	278	$8.05 \times 10^{-4}$	0.10	$150 t^{\frac{1}{2}}$
telescope	278	$8.05 \times 10^{-4}$	0.15	$106 t^{\frac{1}{2}}$
atmosphere	278	$8.05 \times 10^{-4}$	0.40	$69 t^{\frac{1}{2}}$
Total Background <sup>a</sup>	278			$419 t^{\frac{1}{2}}$
Dark Current	50			$650 t^{\frac{1}{2}}$
Johnson Noise <sup>b</sup>	50			$329 t^{\frac{1}{2}}$
Read Noise				$300 t^{-\frac{1}{2}}$

<sup>a</sup> We use Equations 2.2 and 2.3 with  $\lambda_0 = 2.122 \mu\text{m}$ ,  $A\Omega = 3.02 \times 10^{-3} \text{ cm}^2 \text{ st}$ , and  $\eta = 0.6$ .

<sup>b</sup> We use Equation 2.4 with  $R = 10^{12}\Omega$ .

are permanently mounted in two holders. The rear mirror holder is mechanically tilted by adjusting two spring loaded mounting screws. The front mirror holder is attached to a tunable etalon drive ring and three piezoelectric transducers (PZTs) support the drive ring. The PZT is a kind of actuator and an electrically controllable positioning element whose length varies in proportion to the high DC voltage supplied ( $\sim 6 \mu\text{m}$  per 1000 V). Controlling the three PZTs independently aligns the front plate with respect to the rear plate, and driving all three PZTs synchronously changes the plate spacing ( $l$ ) parallel to the optical axis. To manipulate the etalon plates, three alignment voltages (0–500 V) are applied to the negative poles of the PZTs individually and one scan voltage (0–1000 V) is applied to the positive poles simultaneously (Figure 2.3). We can integrate the signal at a fixed scanning voltage and make a spectral

profile by increasing or decreasing the scanning voltage step by step. Because of the crystal characteristics of PZTs, the positive field on each PZT should not exceed 1000 V or the reverse field should not exceed 500 V.

## 2.5 Shortcomings of Fabry–Perot

As we expressed in Equations 2.13 and 2.15, the misalignment of the etalon plates in the FP decreases the net finesse ( $F_{net}$ ) and reduces the spectral resolving power. To keep the value of the net finesse over 90% of the reflectivity finesse ( $F_{net} \simeq 39$ ,  $F_{ref} \simeq 43$ , and neglecting  $F_{ang}$ ), the parallelism (alignment) and planeness finesse ( $F_{pp}$ ) should be over 96, which requires that the deviation from the aligned status be less than  $0.011 \mu\text{m}$ . The corresponding tolerance in aligning voltage is 1.8 V.

A conventional method for alignment is illuminating the FP with a expanded and collimated  $653 \mu\text{m}$  He-Ne laser and looking at the projected interference pattern on a distant screen. For this method we used a commercial control box (Model RC-43, Burleigh Inc.) which has a ramp generating circuit and one amplifying circuit to support three scanning PZTs, and has three power outputs which are adjusted by individual potentiometers to control the alignment. With sequential scanning ramp mode and the reference source, we can see moving interference fringes on the screen. If the two mirrors are aligned well, the fringe pattern becomes a single bright or dark spot. Watching the fringe pattern and with trial and error, we can adjust one of three aligning potentiometers and find the best voltages of the corresponding PZTs in turn.

Surfaces on the reflecting mirrors in our FP, however, are specially

coated for infrared light only. The reflectivity or finesse at visible wavelengths is not sufficient for alignment by eye, and we cannot expect a precise alignment with this method. Another shortcoming of the FP is that the PZTs are not electrically stable and misalign the etalon in  $\sim 10$  minutes. It is very inefficient to align with the conventional method while observing. Thus, we automated the alignment procedure with a closed loop computer controlled method.

## 2.6 High Voltage Amplifier

To manipulate the PZTs, we built a new high voltage DC amplifier, because the RC-43 is inadequate for the automated alignment system. The new amplifier is used between the PZTs and D/A interface board in the computer. Since our D/A board has four 0 to 10 volt output channels, the HV amplifier needs three independent aligning channels with 50 gain and one scanning channel with 100 gain.

Our HV amplifier box has one regulated high voltage supply (Model 602C-15P, Bertan Associates, Inc.) and four independent noninverting feedback amplifier circuits, each of which contains an identical op-amp (Figure 2.3). To make the high voltage output, we put a power transistor between the op-amp and the output channel using the idea of *current sources* (Horowitz and Hill 1989). The gain of each circuit is determined by  $R_1$  and  $R_2$  ( $G = 1 + R_2/R_1$ ). We chose metal film resistors, because they are very accurate and stable with changes in outside temperature.

Another important thing in designing the circuit is the amount of the output power at each channel, because each PZT has capacitance of 2 nano

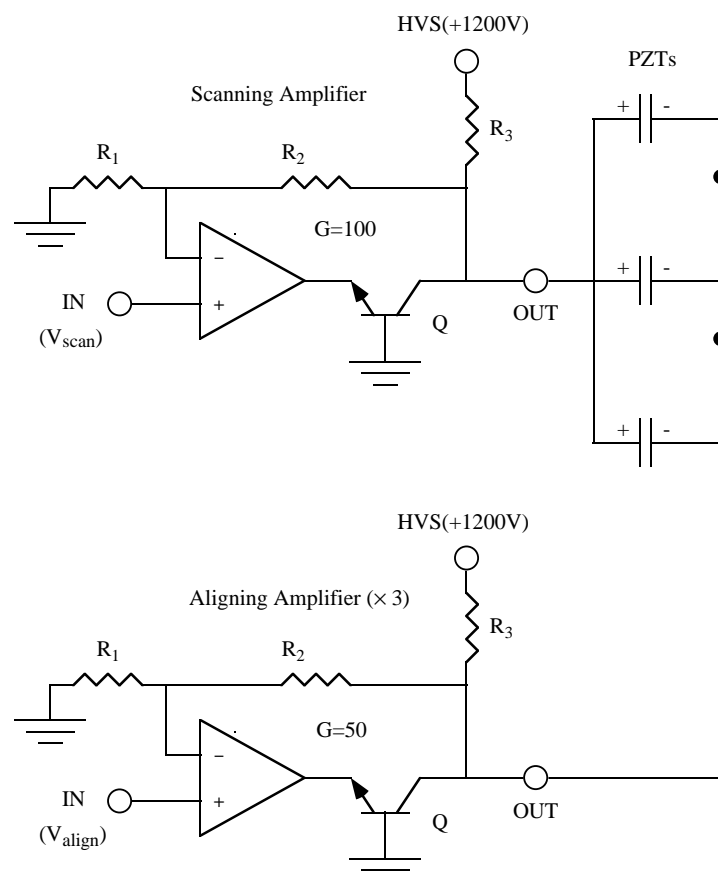


Figure 2.3.— Simplified noninverting feedback op-amplifier circuit diagram for the scanning amplifier and one of the aligning amplifiers. The gain ( $G$ ) is determined by  $G = 1 + R_2/R_1$ . One regulated high voltage supply (HVS) supports all of the four circuits and each  $R_3$  divides the output power.

Farad [nF]. We can simplify the amplifier circuit and the connected PZT with Thévenin's theorem. When a supplied voltage to a PZT is changed (from  $V_i$  to  $V_f$ ), it takes some time for a voltage of the PZT ( $V$ ) to reach the desired voltage,

$$V = V_f + (V_i - V_f) \exp\left(-\frac{t}{ZC}\right), \quad (2.17)$$

where  $Z = R_3 V_f / 1200$ , and  $R_3$  is the load resistor. By decreasing  $R_3$ , we can decrease the response time and increase the output power. Using low resistance load resistors, however, produces another difficulty in finding stable high power resistors. With these restrictions we need to decide on the appropriate output power. The scanning channel supports three parallel PZTs ( $3 \times 2$  nF) and the response time should be less than 5 msec (the interval between resetting the JFET and integrating) to satisfy our requirements for system speed. Each aligning channel supports only one PZT and the voltage changes do not happen frequently. A certain amount of response time ( $\sim 10$  msec) is allowed in this case. Each aligning channel has 0.1 W output power and the scanning channel has 1 W.

## 2.7 Automatic Alignment Program

Part of the FP spectrometer system control program is an automatic alignment routine which can be called frequently and performed quickly. Since the behavior of the PZT is very sensitive to outside conditions and is unpredictable, the simplest procedure (i.e., a *trial and error* method) is safe and convenient. We use a Helium  $2.112\mu\text{m}$  line in a He-Ne laser as a spectral reference source. The program monitors the FP alignment by checking the spectral

profile of the reference source. If the FP etalon plates are not seriously out of alignment, the observed flux of a reference line is almost constant and independent of the alignment. As the two plates become parallel, the full width at half maximum (FWHM) of the observed profile decreases and the peak signal value ( $P_i$ ) increases. We use the peak signal to monitor the alignment.

Figure 2.4 shows the flow chart of the automatic alignment program. At first, the program scans the reference spectral line by changing the voltage of the scanning PZTs ( $V_{scan}$ ). From the scanned data, a peak signal value of the line is stored in a buffer. Next, one of three aligning PZT voltages ( $V_{align1}$ ) is adjusted while fixing the other two voltages ( $V_{align2}$  and  $V_{align3}$ ), and the reference line is scanned again. The amount of adjusting voltage ( $\Delta V$ ) is the same as the aligning voltage tolerance (1.8 V) which we deduced in section 2.5. If the new peak value is larger than the previous one, the program adjusts the aligning voltage and scans again. This is repeated until the FP is aligned. With this routine, the other two aligning voltages can be adjusted in turn. It takes less than 30 seconds to align with this program. We call this alignment routine every 5 – 10 minutes during observations.

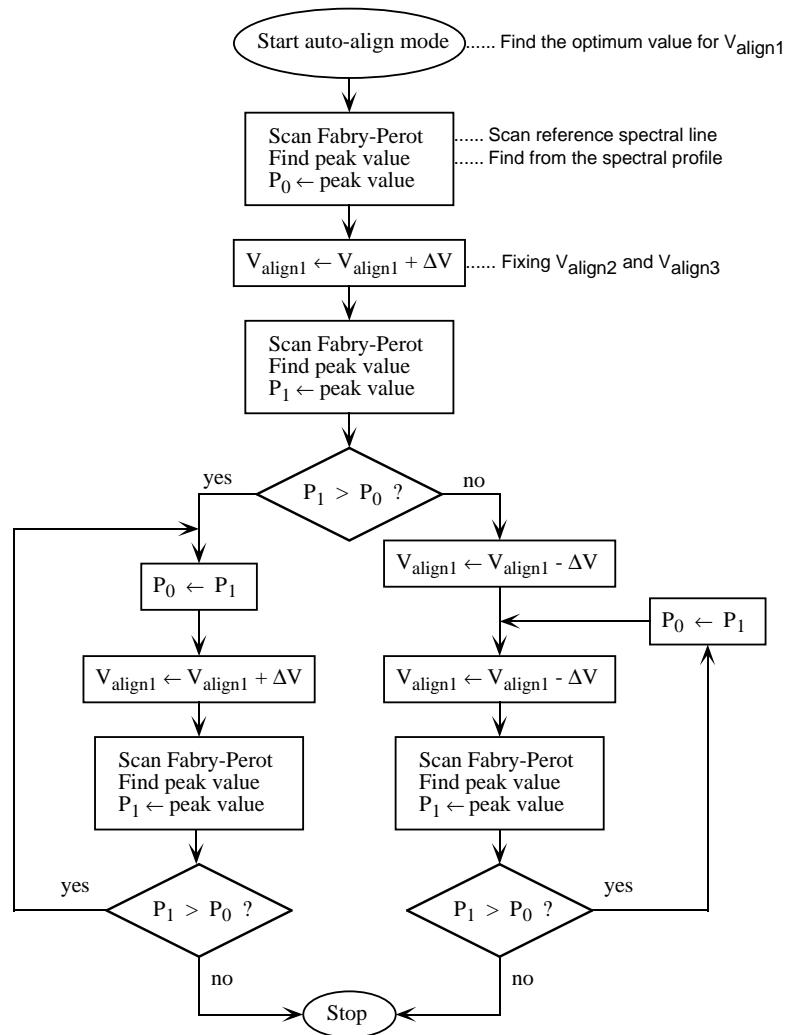


Figure 2.4.— The algorithm of the automatic alignment program. A trial and error approach is used to find the best  $V_{align1}$ . The program monitors the aligned status by checking the peak signal value ( $P_i$ ) of the observed reference spectral profile. Running this routine for  $V_{align2}$  and  $V_{align3}$  in turn, the FP spectrometer system can maintain optimum alignment.

## Chapter 3

### OBSERVATIONS

We observed the  $\text{H}_2$   $v = 1 \rightarrow 0$   $S(1)$  ( $\lambda = 2.122\mu\text{m}$ ) transition line in bipolar molecular outflows using the UT FPS on the 2.7 m telescope at McDonald Observatory. The description of the UT FPS is in Chapter 2 and in a later paper (Luhman et al. 1994). For Cepheus A, we observed 30 points covering major parts of the outflow region (based on CO observations; Rodríguez, Ho, and Moran, 1980), and for L1448 we measured four points along the blueshifted northern lobe in 1992 October. A sample part of L1551 was also observed in 1992 December.

With the beam size of  $49''$ , we obtained spectra by scanning the Fabry-Perot across the  $\text{H}_2$  2.122  $\mu\text{m}$  line at each position. In the scanned spectrum, 25 channels were sequentially exposed and the step size between channels was  $30 \text{ km s}^{-1}$ . The spectral resolution from the instrument profile was  $\Delta v \sim 130 \text{ km s}^{-1}$  with the measured net finesse of  $F_{net} \sim 25$  (see Equations 2.15 and 2.16). As we discussed in Section 2.7, we aligned the Fabry-Perot plates every 5 – 10 minutes by monitoring the reference spectral line and we calibrated the wavelength scale by scanning the same reference line. In 1992 October the reference line was a He 2.112  $\mu\text{m}$  line from the He-Ne laser discharge. Jumping between  $\text{H}_2$  2.122  $\mu\text{m}$  and He 2.112  $\mu\text{m}$ , however, resulted in drift of the scanning PZT and the uncertainty of the wavelength scale became about

60 km s<sup>-1</sup>. In 1992 December we changed the reference line to an unidentified spectral line ( $2.1225 \pm 0.0002 \mu\text{m}$ ) in the same He-Ne laser, and this minimized the PZT drift ( $\sim 30 \text{ km s}^{-1}$ ) in the L1551 data.

## Chapter 4

### RESULTS

#### 4.1 Cepheus A

Cepheus A is a region of massive star formation in the molecular cloud southeast of the Cepheus OB3 association. It contains a far-infrared source, radio HII regions, OH and H<sub>2</sub>O maser sources, and shock-excited Herbig-Haro objects (see review by Lane 1989). High velocity CO observations have revealed an east-west bipolar morphology with dominant blueshifted gas to the east (Rodríguez, Ho, and Moran 1980). Recent high spatial and spectral resolution observations in the NH<sub>3</sub>(1,1) and NH<sub>3</sub>(2,2) lines have suggested a complex quadrupolar morphology. (Torrelles, Verdes-Montenegro, and Ho 1993).

Bally and Lada (1982) first detected the H<sub>2</sub>  $v = 1 \rightarrow 0$   $S(1)$  ( $\lambda = 2.122 \mu\text{m}$ ) emission lines from the peak in the eastern lobe of Cepheus A. Doyon and Nadeau (1988, hereafter DN88) observed the H<sub>2</sub> line with a high spectral resolution ( $\sim 20 \text{ km s}^{-1}$ ) Fabry-Perot spectrometer, and suggested that the FWHM of the deconvolved spectra at the peak positions is in the range of  $15 - 45 \text{ km s}^{-1}$ . The shape of the H<sub>2</sub> spectral profiles gives very important information on the MHD shock model. In the case of *C - type* shocks (see the review in Chapter 1), molecular hydrogen is not dissociated and the neutral flow is continuous at the shock front, so that the observed emission lines are broadened by the velocity distribution in the cooling regions

(Hollenbach, Chernoff, and McKee 1989). Based on the spectra of DN88, the shock in Cepheus A is *C - type*.

DN88 also made a map of H<sub>2</sub> 2.122  $\mu\text{m}$  emission with a  $7'' \times 23''$  rectangular beam. Their map, however, covered only a small region (total  $2' \times 1'$ ) around peak positions in eastern and western lobes. With a 1% bandpass filter, Bally and Lane (1990, and Lane 1989) made a high angular resolution map of H<sub>2</sub> emission and discussed the morphology of the shocked regions (see Section 2.1). Their detections, however, were contaminated by continuum emission and they could not calibrate the line flux from the source.

The four spectra in Figure 4.1 show the observed velocity profile of the H<sub>2</sub> 2.122  $\mu\text{m}$  emission lines. Though our spectrometer does not have enough resolution to resolve the H<sub>2</sub> lines, we can calibrate the flux from the lines. Figure 4.2 is a map of the intensity of H<sub>2</sub> emission toward the bipolar lobes in Cepheus A. The plotted numbers are in the units of  $10^{-5} \text{ erg s}^{-1} \text{ cm}^{-2} \text{ sr}^{-1}$  and the plus (+) signs are observations below  $3\sigma$  level ( $3\sigma \simeq 1.4 \times 10^{-5} \text{ erg s}^{-1} \text{ cm}^{-2} \text{ sr}^{-1}$  with an integration time of 4 seconds per channel). The coordinate offsets are relative to  $\alpha_{1950} = 22^{\text{h}} 54^{\text{m}} 19^{\text{s}}.9$ ,  $\delta_{1950} = 61^{\circ} 45' 56''$  which roughly corresponds to the 20  $\mu\text{m}$  peak position (Beichman, Becklin, and Wynn-Williams 1979; Bally and Lane 1982). A bright IR reflection nebula, inside of which a series of compact HII regions were identified, lies at the peak of the eastern blueshifted lobe (Bally and Lane 1990). We can see the continuum emission at the lower two spectra, 0'' and E30'', in Figure 4.1. The second peak (E90'', N30'') in the blueshifted lobe corresponds to the Herbig-Haro object, HH-NE, identified by Lenzen (1988). The redshifted lobe includes the Herbig-

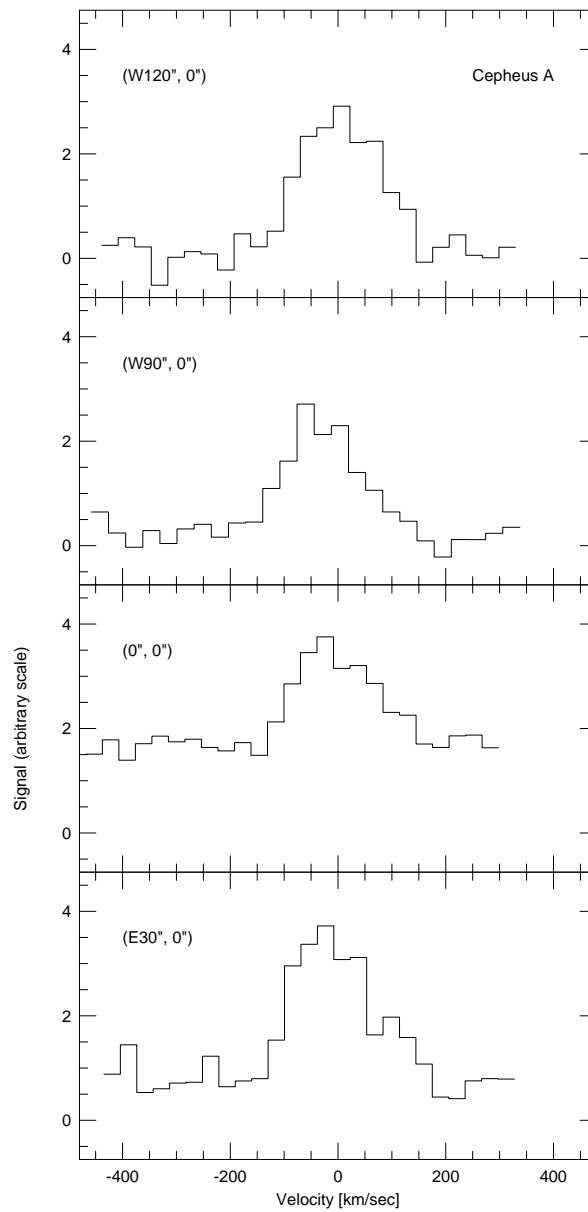


Figure 4.1.— The observed spectra of the  $\text{H}_2 v = 1 \rightarrow 0 S(1)$  ( $\lambda = 2.122\mu\text{m}$ ) emission lines in Cepheus A. These profiles are not deconvolved and are affected by the drifting of PZTs in the Fabry-Perot interferometer.

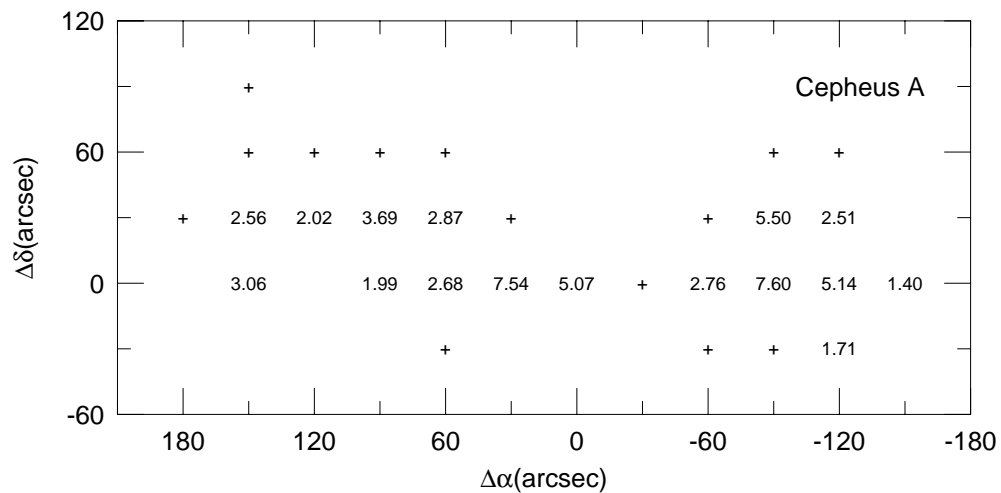


Figure 4.2.— The intensity map of  $\text{H}_2$  2.122  $\mu\text{m}$  emission toward the bipolar lobes in Cepheus A. The plotted numbers are in the units of  $10^{-5} \text{ erg s}^{-1} \text{ cm}^{-2} \text{ sr}^{-1}$  and the plus(+) signs are detections below  $3\sigma$  level ( $\sigma \simeq 0.5 \times 10^{-5} \text{ erg s}^{-1} \text{ cm}^{-2} \text{ sr}^{-1}$ ). The coordinate offsets are relative to  $\alpha_{1950} = 22^{\text{h}} 54^{\text{m}} 19^{\text{s}}.9$ ,  $\delta_{1950} = 61^{\circ} 45' 56''$  which roughly corresponds to the  $20\mu\text{m}$  peak position (Bally and Lane 1982). The telescope pointing to the position is not accurate. We have to allow about  $30''$  error on the spatial position.

Haro object GGD 37 (Lane 1989).

## 4.2 L1448

L1448 is a dense molecular cloud core located about  $1^\circ$  southwest of NGC 1333, in the local complex of dark clouds in Perseus. The Infrared Astronomical Satellite (IRAS) identified 3 infrared sources (IRS 1, 2, and 3) associated with L1448 (Bachiller and Cernicharo 1986). IRS 3 is the brightest far-infrared object and a compact HII region and a strong  $\text{H}_2\text{O}$  maser have been detected near it. Bachiller et al. (1990) discovered very rapid and highly collimated outflowing molecular gas (main outflow) from the *U*-star (unseen star, denoted by Bachiller et al. 1990) southeast ( $+35''$ ,  $-75''$ ) of IRS 3. IRS 3 is embedded in the end of this main outflow. The source of the bipolar outflow, U-star, coincides with the cm- and mm- wavelength source, and it is believed to be one of the youngest YSO's known (Bally, Lada, and Lane 1993, hereafter BLL93). Also, there is another less energetic and smaller outflow (second outflow), which seems to be excited by IRS 3 itself. Terebey (1991) detected  $\text{H}_2$   $2.122\mu\text{m}$  emission around IRS 3. BLL93 obtained images of L1448 with a 1% passband filter centered on  $2.122\mu\text{m}$  and a K-band filter.

Figure 4.3 shows spectra along the axis of the northern blueshifted outflow lobe from U-star. The coordinate offsets are relative to IRS 3 ( $\alpha_{1950} = 3^h 22^m 31^s.5$ ,  $\delta_{1950} = 30^\circ 34' 49''$ ). The main outflow source, U-star, is included in the bottom spectrum (E33'', S84''), but its continuum intensity is below our instrument sensitivity limit ( $3\sigma = 0.5 \times 10^{-5} \text{ erg s}^{-1} \text{ cm}^{-2} \text{ sr}^{-1}$  with an integration time of 8 seconds per channel). The spectrum at  $0''$ ,  $0''$  is contaminated

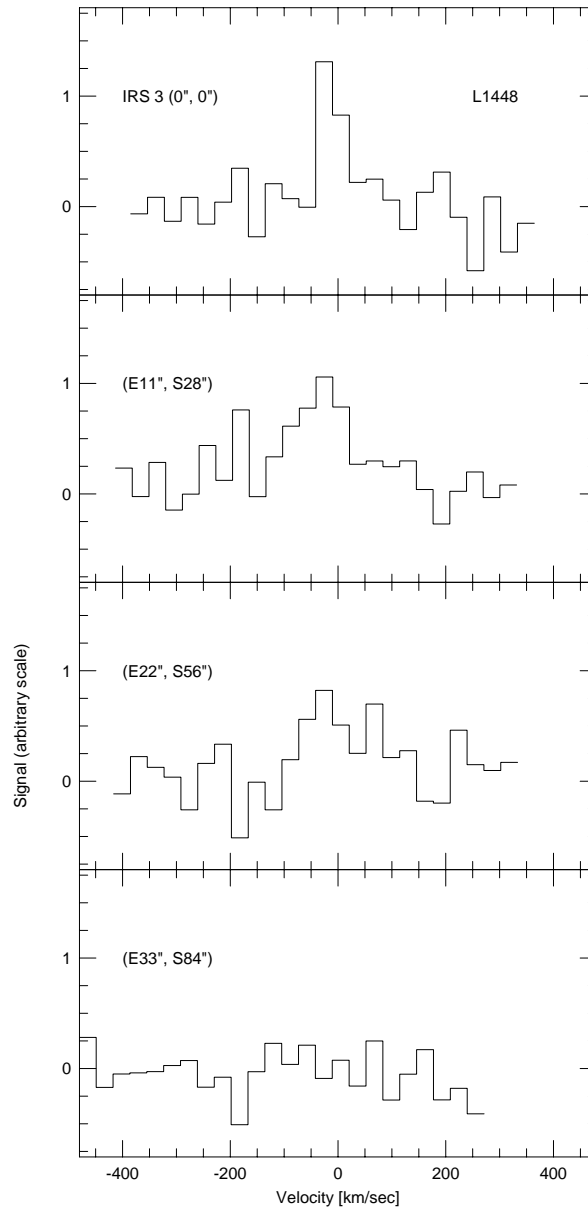


Figure 4.3.— Spectra of the northern blueshifted outflow lobe in L1448. The coordinate offsets are relative to the positions of IRS 3 ( $\alpha_{1950} = 3^h 22^m 31^s.5$ ,  $\delta_{1950} = 30^\circ 34' 49''$ ). Note the shape of the spectral profile at  $0''$ ,  $0''$  which is different from those of other positions.

by the other IRS 3 outflow, but high spatial resolution observations by BLL93 showed that the  $\text{H}_2$   $2.122\mu\text{m}$  luminosity from the IRS 3 outflow is  $\sim 10\%$  of that from the U-star outflow. It is noticeable that the shape of the spectral profile at  $0''$ ,  $0''$  is remarkably narrower than that of the spectra in Cepheus A (Figure 4.1) which were obtained at the same night as L1448.

### 4.3 Evidence for Diffuse Emission in L1551

L1551/IRS 5 is the first outflow source observed to have a bipolar pattern (Snell, Loren, and Plambeck 1980), and the most well-studied low mass star formation region. Moriarty-Schieven and Snell (1988, hereafter MS88) presented a complete map of the high-velocity  $^{12}\text{CO}$  emission with a  $45''$  beam and calculated the total momentum in the cold molecular gas to be  $15.6 M_{\odot} \text{ km s}^{-1}$  without considering inclination. Even though they modeled the molecular outflow as an expanding shell with an evacuated interior cavity, clumpy structure and the existence of three Herbig-Haro objects (HH 28, 29, and 30) makes modeling the MHD shock structure complex. Yamashita and Tamura (1992) detected  $\text{H}_2$   $2.122\mu\text{m}$  emission at L1551/IRS 5. No previous observation, however, has succeeded in detecting the  $\text{H}_2$  emission from the lobes because the lobes are so extended ( $10' \times 30'$ ) and diffuse.

We observed L1551 and collected some sample data along the axis of the southwestern blueshifted lobe. We can compare our data with the CO map in Moriarty-Schieven and Snell 1988, and expect to see the  $\text{H}_2$  emission from the intersection of the outflow lobe and the ambient gas (see Section 2.1). Figure 4.4 shows the averaged spectrum of the intersection region,  $11' - 16'$  away

from IRS 5. The averaged surface brightness of the region is  $2.7 \times 10^{-6} \text{ erg s}^{-1} \text{ cm}^{-2} \text{ sr}^{-1}$ , and the signal to noise ratio is 3.4 with a total integration time of 18 seconds per channel. There is no Herbig-Haro object identified in the region. This implies that the cooling regions are very faint and extended, which is totally different from the previous  $\text{H}_2$  observations of the other outflows. Most of the  $\text{H}_2$  sources have been identified as Herbig-Haro objects which are very compact and luminous and are believed to be excited by highly collimated jets (BLL93).

#### 4.4 Shocked $\text{H}_2$ Luminosity

We calibrated the  $\text{H}_2 v = 1 \rightarrow 0 S(1) (\lambda = 2.122 \mu\text{m})$  line flux from the redshifted lobe of Cepheus A as  $5.62 \times 10^{-12} \text{ erg s}^{-1} \text{ cm}^{-2}$ , from the blueshifted lobe of Cepheus A as  $6.66 \times 10^{-12} \text{ erg s}^{-1} \text{ cm}^{-2}$ , and from the blueshifted lobe of L1448 as  $9.82 \times 10^{-13} \text{ erg s}^{-1} \text{ cm}^{-2}$ . BLL93 measured the continuum-subtracted line luminosities in L1448,  $3.2 \times 10^{-3} L_\odot$  from the blueshifted lobe and  $1.8 \times 10^{-3} L_\odot$  from the redshifted lobe without an extinction correction. Our value ( $2.7 \times 10^{-3} L_\odot$ ) of the blueshifted lobe in L1448 agrees with that of BLL93 within a 15% error margin. The corresponding line luminosities ( $L_{2.122}$ ) are listed in Table 4.1 after correcting for extinction ( $A_{2.122}$ ). We have to allow that our detections are still just suggesting the minimum luminosity values, because we are not sure how extended the sources are. In order to extrapolate from the one line luminosity to the total  $\text{H}_2$  radiative energy, we define the fraction of the 2.122  $\mu\text{m}$  luminosity to the total  $\text{H}_2$  luminosity,

$$R_{2.122} = \frac{I_{(v=1, J=3), (v'=0, J'=1)}}{\sum I_{vJ, v'J'}}. \quad (4.1)$$

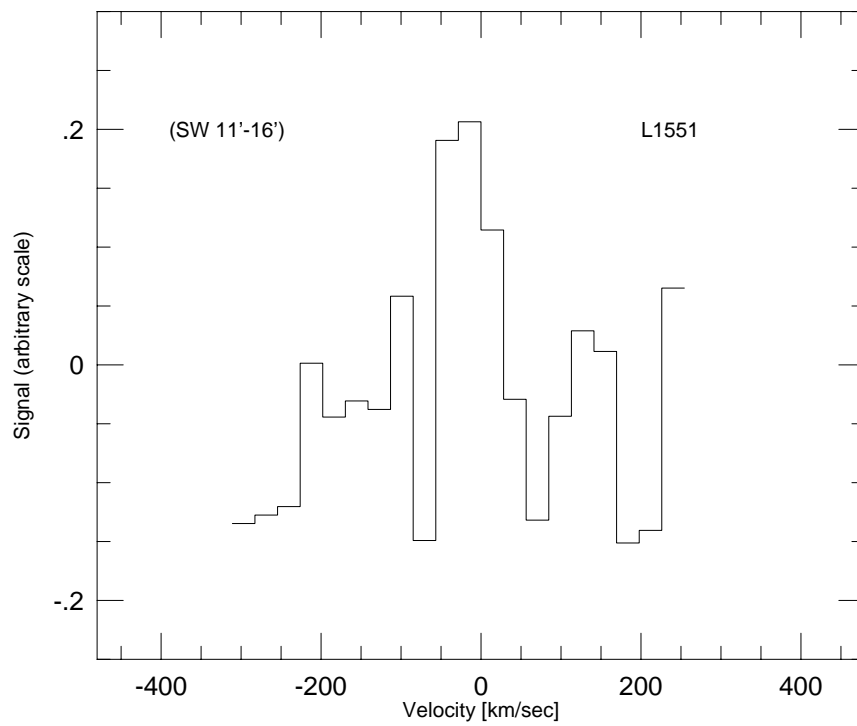


Figure 4.4.— The averaged spectrum of L1551. The sample detections along the region 11'–16' away from IRS 5 are averaged to increase the sensitivity. The surface brightness of the region is  $2.7 \times 10^{-6}$  erg s $^{-1}$  cm $^{-2}$  sr $^{-1}$  and the signal to noise ratio is 3.4 with the total integration time of 18 sec.

We need to know the thermodynamic status of the shocked regions to get  $R_{2,122}$ .

TABLE 4.1  
H<sub>2</sub> and Total Luminosity

objects	distance [pc]	lobe	A <sub>2,122</sub> [mag]	L <sub>2,122</sub>	L <sub>H2</sub> [L <sub>⊙</sub> ]	L <sub>tot</sub>	physical situation <sup>a</sup>
Cepheus A	725 <sup>(2)</sup>	blue	1.8 <sup>(3)</sup>	0.565 <sup>(1)</sup>	7.7	34	C-2 <sup>b</sup>
		red	1.8	0.477	6.5	28	
L1448	300 <sup>(4)</sup>	blue	1 <sup>(5)</sup>	0.0068 <sup>(1)</sup>	0.26	0.35	C-1
		red	2 <sup>(5)</sup>	0.011 <sup>(5)</sup>	0.42	0.56	
L1448		blue			0.093	0.41	C-2
		red			0.15	0.66	
L1448		blue			0.12	1.5	J-1
		red			0.19	2.4	
L1448		blue			0.076	76	J-2
		red			0.12	122	

<sup>a</sup> The physical situation in case 1 is ( $n_H = 10^4 \text{ cm}^{-3}$ ,  $v_{shock} = 30 \text{ km s}^{-1}$ ,  $x_e = 10^{-7}$ , and  $B_o = 0.05 \text{ mG}$ ), and the physical situation in case 2 is ( $n_H = 10^6 \text{ cm}^{-3}$ ,  $v_{shock} = 30 \text{ km s}^{-1}$ ,  $x_e = 10^{-8}$ , and  $B_o = 0.5 \text{ mG}$ ). See the text in Section 4.4.

<sup>b</sup> The shock model is *C-type* in the physical situation of case 2

References. — (1) This paper (2) Blaauw, Hiltner, and Johnson 1959 (3) Doyon and Nadeau 1988 (4) Bachiller and Cernicharo 1986 (5) Bally, Lada, and Lane 1993

If we suppose the cooling gas is approximately in local thermodynamic equilibrium (LTE), we can simply calculate the value of  $R_{2,122}$ . With an excitation temperature ( $T_{exc}$ ) the individual line intensity ratio is,

$$\frac{I_{U1,L1}}{I_{U2,L2}} = \frac{A_{U1,L1}}{A_{U2,L2}} \frac{E_{U1} - E_{L1}}{E_{U2} - E_{L2}} \frac{g_{U1}}{g_{U2}} \exp\left(-\frac{E_{U1} - E_{U2}}{k T_{exc}}\right), \quad (4.2)$$

where  $I_{U_i,L_i}$  is the emission line intensity of transition from the upper  $U_i$  level to the lower  $L_i$  level,  $A_{U_i,L_i}$  is the quadrupole vibration-rotation transition probability (Turner, Kirby-Docken, and Dalgarno 1977), and  $E_{U_i}$  and  $E_{L_i}$  are the

upper and lower energy levels (Dabrowski 1984). The total statistical weight,  $g_{U_i}$ , is from rotational and spin degeneracy at the upper level,

$$g_{U_i} = (2J_{U_i} + 1)(2I_{U_i} + 1), \quad (4.3)$$

where  $J_{U_i}$  is the rotational quantum number and  $I_{U_i}$  is the total nuclear spin quantum number ( $I_{U_i} = 0$  for the para- $\text{H}_2$  state and  $I_{U_i} = 1$  for the ortho- $\text{H}_2$  state). DN88 measured the line intensities of  $v = 1 \rightarrow 0 S(1)$  and  $v = 2 \rightarrow 1 S(1)$  at the peak position of the western lobe in Cepheus A, and they deduced the  $T_{exc}$  as  $2400 \pm 300$  K from the line ratio. With Equation 4.2 and the single value of  $T_{exc}$  in DN88, the  $R_{2.122}$  is  $0.07 \pm 0.01$ . In this LTE model the dominant cooling is due to the  $v = 1 \rightarrow 0$  vibrational transitions, so that the value of the  $R_{2.122}$  is not very sensitive to the excitation temperatures.

Unfortunately, the real shocked gas would not be in LTE and our understanding of the shock mechanism is considerably uncertain. Two basic forms of shock model have been proposed, jump ( $J$ -type) shock and continuous ( $C$ -type) shock. Based on  $C$ -type shock model, DRD83 numerically calculated the physical structure of the shock front and estimated the individual quadrupole transition line intensities of  $\text{H}_2$ . Applying the result of DRD83 with two typical situations in the preshock gas, we get  $R_{2.122}$  as 0.026 in case 1 ( $n_H = 10^4 \text{ cm}^{-3}$ ,  $v_{shock} = 30 \text{ km s}^{-1}$ ,  $x_e = 10^{-7}$ , and  $B_o = 0.05 \text{ mG}$ ), and as 0.073 in case 2 ( $n_H = 10^6 \text{ cm}^{-3}$ ,  $v_{shock} = 30 \text{ km s}^{-1}$ ,  $x_e = 10^{-8}$ , and  $B_o = 0.5 \text{ mG}$ ), where  $n_H$  is the number density of hydrogen in the preshock gas,  $x_e$  is the ionization fraction, and  $B_o$  is the ambient magnetic field strength. The value of  $R_{2.122}$  is sensitive to the physical situation in the  $C$ -type shock model at the factor of three level.

Hollenbach and McKee (1989) presented another type of shock model, *J* – *type* shock, in which the shock front is treated as a discontinuity and ambipolar diffusion is negligible. From their result,  $R_{2.122}$  is 0.058 in case 1 and 0.090 in case 2. Because most of the hydrogen molecules are dissociated at the shock front, the *J* – *type* shock model includes UV pumping and H<sub>2</sub> formation pumping in calculating populations. The value of  $R_{2.122}$  in *J* – *type* shock is not as sensitive to the physical situation as in *C* – *type* shock. The predicted line intensity ratio of  $v = 2 \rightarrow 1 S(1)$  to  $v = 1 \rightarrow 0 S(1)$  in the *J* – *type* shock model is about 0.5.

It is difficult to apply this *J* – *type* model to the the previous observational results in Cepheus A, i.e., the ratio of  $v = 2 \rightarrow 1 S(1)$  to  $v = 1 \rightarrow 0 S(1)$  was measured as 0.13 by DN88. If we apply the only information (the line ratio of 0.13) of DN88 to the *C* – *type* model (DRD83), the shock in Cepheus A is in the physical situation of case 2. We assume that  $R_{2.122}$  is 0.073 for Cepheus A. Since there has been no H<sub>2</sub> emission line detection toward L1448 except for the 2.122  $\mu\text{m}$  line, there is no justification for extrapolation. We apply all the situations (case 1 and case 2 in *C* – *type* and *J* – *type*) to L1448. These results are listed in Table 4.1.

## 4.5 Shocked Total Luminosity

We need another extrapolation from the H<sub>2</sub> luminosity to the total shocked luminosity, because the H<sub>2</sub> is not always the dominant coolant. We define  $R_{H_2}$ , the fraction of the H<sub>2</sub> luminosity to the total luminosity. The other important cooling lines are the rotational lines of H<sub>2</sub>O and OH which are

impossible to detect from ground based telescopes, and the fine-structure lines (63  $\mu\text{m}$  and 146  $\mu\text{m}$ ) of OI which may be observed on an airborne observatory. Since there are no data on these cooling emission lines, we have to rely upon the shock models again. For the *C-type* shock model by DRD83,  $\text{H}_2$  is dominant in the diffuse cloud shocks ( $n_H = 10^2 \text{ cm}^{-3}$ ). In more dense regions ( $n_H \geq 10^4 \text{ cm}^{-3}$ ), however,  $\text{H}_2\text{O}$  rotational lines begin to contribute strongly.  $R_{\text{H}_2}$  is 0.75 in the physical situation of the case 1, but  $R_{\text{H}_2}$  is only 0.23 in the case 2.

The *J-type* shock model by Hollenbach and McKee (1989) has a different prediction of the power in the coolant species. In their model, the  $\text{H}_2$  is completely dissociated at the shock front, and the radiative cooling of the gas is partially offset by heating due to absorption of UV radiation from the hot gas and due to the release of chemical energy by the formation of  $\text{H}_2$ . The grains,  $\text{H}_2\text{O}$ , OH, and OI are more important coolants, especially, in high density gas ( $n_H = 10^6 \text{ cm}^{-3}$ ). In the physical situation of case 1 and case 2, the values of  $R_{\text{H}_2}$  are 0.08 and 0.001 respectively.

## Chapter 5

### DISCUSSION

#### 5.1 Stellar Wind as Outflow Source

It is believed that during the first evolutionary stages of star formation, the forming star generates a very fast, well-collimated, bipolar wind that sweeps up the ambient gas in its vicinity, forming two cavities oriented in opposite directions (see the review by Bachiller and Gómez-González 1992). We can assume that the supersonic wind is ejected from the YSO with a steady mass loss rate of  $\dot{M}_w$  and velocity of  $v_w$  to the ambient molecular cloud. Shu et al. (1991) proposed that the cloud core density distribution around the YSO is,

$$\rho(r, \theta) = \frac{a^2}{2\pi Gr^2} Q(\cos \theta), \quad (5.1)$$

where  $a$  is the effective sound speed of the cloud core, and  $Q(\cos \theta)$  yields the flattening of density contours that arises either because of partial support against self-gravitation by rotation or by magnetic fields ( $Q(1)/Q(0) \sim 1/4$ ). As the density decreases more steeply in a direction perpendicular to the plane, the ejected material moves faster in the direction, which may produce a collimated structure in the bipolar molecular outflow.

## 5.2 Energy Conserving Model and Momentum Conserving Model

When the supersonic wind encounters the circumstellar material, a shock front will be generated and begin to sweep up the ambient interstellar medium. This shock front is likely to be isothermal, and a high density shell will be formed at the shock front. From the shock front, two shock waves are found : the *ambient shock* advances into the ambient interstellar medium at velocity  $v_{sa}$ , and the *wind shock* moves backward at a velocity  $v_{sw}$  relative to the outflowing wind ( $v_w = v_{sw} + v_{sa}$ ). If the shocked stellar wind is radiative and the wind flow is isothermal, most of wind energy is lost by radiation and only *momentum* is conserved. On the contrary, if the stellar wind is shocked by the wind to high temperature and cannot radiate away the excess thermal energy, the outflow is filled with a hot, high pressure gas. The pressure inside the lobes inflates bubbles, producing large transverse and longitudinal velocities in this *energy* conserving model.

The model of the momentum conserving flow is based on the assumptions that both the wind shock and ambient shock are radiative, and that the flow is isothermal and entirely radial, i.e., transverse motions of the shocked gas are negligible. McKee and Hollenbach (1987) analyzed the dynamical model for a steady wind (outflow) confined to a solid angle ( $\Omega$ ) expanding into a uniform ambient medium of density  $\rho_a$ . They split the mass of the wind ( $M_w$ ) into two : the mass in the unshocked wind,

$$M_{uw} = \frac{R}{v_w} \dot{M}_w, \quad (5.2)$$

and the mass in the shocked wind,

$$M_{sw} = \left(t - \frac{R}{v_w}\right) \dot{M}_w, \quad (5.3)$$

where  $R$  is the radius of the shock front at time  $t$  ( $dR/dt = v_{sa}$ ) and  $\dot{M}_w$  is  $dM_w/dt$ . The mass in the shocked ambient gas is,

$$M_{sa} = \frac{\Omega}{3} \rho_a R^3. \quad (5.4)$$

Momentum conservation for the above mass motions leads to the following relation,

$$\dot{M}_w v_w t = \dot{M}_w R + \dot{M}_w \left(t - \frac{R}{v_w}\right) v_{sa} + \frac{\Omega}{3} \rho_a R^3 v_{sa}. \quad (5.5)$$

To simplify these expressions, we introduce the dimensionless variable ( $\xi = R/R_{ch}$ ) and the characteristic radius ( $R_{ch}$ ),

$$R_{ch} = \left(\frac{6\dot{M}_w}{\Omega\rho_a v_w}\right)^{\frac{1}{2}} \approx 0.13 \left(\frac{\dot{M}_{w-4}}{\Omega n_{a4} v_{w2}}\right)^{\frac{1}{2}} \text{ pc}, \quad (5.6)$$

where  $\dot{M}_{w-4}$ ,  $n_{a4}$  and  $v_{w2}$  are in the units of  $10^{-4} M_{\odot} \text{ yr}^{-1}$ ,  $10^4 \text{ cm}^{-3}$ , and  $10^2 \text{ km s}^{-1}$  respectively. The characteristic radius ( $R_{ch}$ ) corresponds to the radius of the shell inside which the density of the expanding wind is comparable to the density of the ambient medium. The total energetics of a massive, radiative wind,  $E_{tot} = M_w v_w^2 / 2$ , can be broken into four parts : (i) the energy of the unshocked wind,  $E_{uw} = M_{uw} v_w^2 / 2$ , (ii) the energy of the shocked wind,  $E_{sw} = M_{sw} v_{sw}^2 / 2$ , (iii) the energy of the shocked ambient gas,  $E_{sa} = M_{sa} v_{sa}^2 / 2$ , and (iv) the radiative energy by the shock,  $E_{rad}$ . The fractions of the energy parts plotted in Figure 5.1 are the following functions :

$$\frac{E_{uw}}{E_{tot}} = \frac{1}{1 + \xi}, \quad (5.7)$$

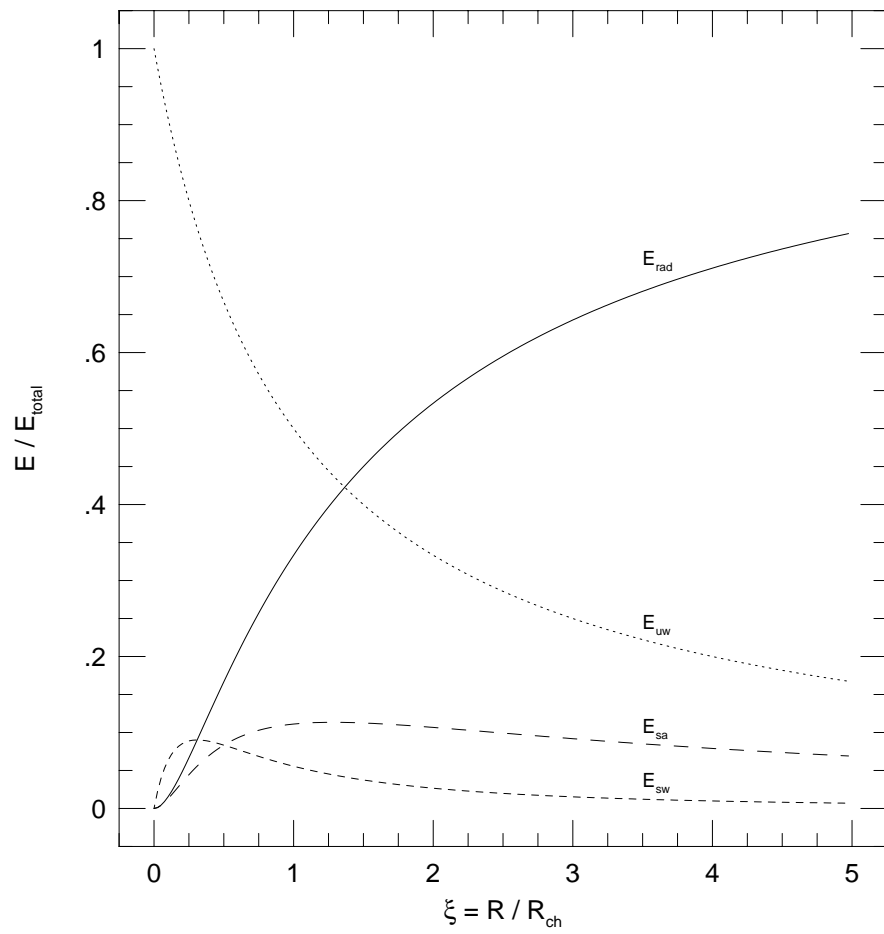


Figure 5.1.— The fraction of the energy parts in the momentum conserving outflow model of McKee and Hollenbach (1987).

$$\frac{E_{sw}}{E_{tot}} = \frac{\xi}{(1 + \xi)(1 + 2\xi)^2}, \quad (5.8)$$

$$\frac{E_{sa}}{E_{tot}} = \frac{2\xi^2}{(1 + \xi)(1 + 2\xi)^2}, \quad (5.9)$$

and

$$\frac{E_{rad}}{E_{tot}} = \frac{2\xi^2}{(1 + \xi)(1 + 2\xi)}. \quad (5.10)$$

For example, at  $\xi \approx 10$ , the kinetic energy of the shocked ambient gas is only 5 % of the total wind energy and the rest of the energy is radiated away.

Kwok and Volk (1985) argued that the temperature in the shocked lobe is so high ( $\sim 10^6$  K) that the gas is fully ionized and the cooling rate is very low. Based on this energy conserving assumption, they calculated the energetics of the wind with a spherical isotropic density distribution model of the cloud. The expected momentum efficiency is,

$$\frac{P_{sa}}{P_w} = \frac{M_{sa}v_{sa}}{\dot{M}_w v_w t} \approx 10^2, \quad (5.11)$$

and the energy efficiency is,

$$\frac{E_{sa}}{E_{tot}} = \frac{M_{sa}v_{sa}^2}{\dot{M}_w v_w^2 t} \approx 0.3. \quad (5.12)$$

The momentum of the swept-up material can rise up to two orders of magnitude if the expansion of the swept-up shell is due to thermal pressure from a hot shocked stellar wind. A third of the total wind energy is converted to the ambient kinetic energy (Equation 5.12). Though we subtract the rest of the energy by the unshocked wind energy ( $E_{uw}$ ), about a half of the total energy is lost by radiation.

### 5.3 Comparing the Models with the Observation

We may test whether the outflow is momentum conserving or energy conserving, if we can observe the radiative energy in the shock, the kinetic energy of the wind, and the kinetic energy of the shocked ambient material. The swept-up mass ( $M_{sa}$ ) and the velocity ( $v_{sa}$ ) are measured by tracing high-velocity emission from the low-J transitions of CO molecules. Quantitative measurements of  $v_w$  and  $M_w$ , however, are difficult because the young stellar objects are deeply embedded in molecular clouds. Lizano et al. (1988) and Giovanardi et al. (1992) detected a neutral atomic wind in the 21 cm line of atomic hydrogen in two bipolar sources, HH 7–11 and L1551. Assuming the winds are neutral, they measured the values of  $v_w$  and  $M_w$ , and deduced the momenta and energies of the winds. Comparing with the CO data, they concluded that the outflow is momentum conserving.

Although the neutral winds of Cepheus A and L1448 have not been detected yet, we can roughly test the models with the CO data of the swept-up molecular outflows and our shocked luminosity data ( $L$ ). If we apply the momentum conserving model with  $\xi \approx 10$  in Equations 5.9 and 5.10, the energy ratio of the radiation and the shocked ambient gas is

$$\frac{E_{rad}}{E_{sa}} = 1 + 2\xi \approx 20. \quad (5.13)$$

In the energy conserving model, we can neglect the kinetic energies of the shocked and unshocked wind ( $E_{sa} \gg E_{uw}, E_{sw}$ ), because the momentum of the swept-up gas is two orders of magnitude larger than that of the stellar wind

(Equation 5.11). From Equation 5.12 the energy ratio is,

$$\frac{E_{rad}}{E_{sa}} \approx 1.5. \quad (5.14)$$

The values of  $E_{rad}$  assume that the luminosity ( $L_{tot}$ ) has been constant over the outflow life time ( $\tau = R/v_{sa}$ ),

$$E_{rad} = \tau L_{tot}. \quad (5.15)$$

The age, the momentum, and the kinetic energy of the outflow, however, are not trivial parameters. Cabrit and Bertout (1992) pointed out many problems and uncertainties in the observation of CO. The outflow does not have a nice shell shape, especially in Cepheus A. In Table 5.1 we list published CO data and our derived radiation energies and show the energy ratio ( $E_{rad}/E_{CO}$ ) in order to test the outflow energetics.

In Cepheus A, the energy ratio based on the data by Levreault (1988) exceeds that of the expected momentum conserving model. Allowing several sources of errors, this result suggests that the outflow is in the momentum conserving regime. Two other CO data sets, however, lead to the energy conserving model. We need more reliable CO observations to analyze the model to analyze the models.

In L1448, we can exclude the physical situation of case 2 in the  $J$ -type shock model (J-2), because we may overestimate the shocked total luminosity. If the shock is  $C$ -type, it is clear that the outflow is in the energy conserving regime. Even in the physical situation of case 1 in the  $J$ -type shock model, the thermal energy inside the lobe still works to convert the shock wind energy to the ambient kinetic energy.

TABLE 5.1  
Outflow Kinetic Energy and Radiation Energy

objects	age <sup>a</sup> [10 <sup>3</sup> yr]	$P_{CO}$ <sup>a</sup> [M <sub>⊙</sub> km s <sup>-1</sup> ]	$E_{CO}$ <sup>a</sup> [10 <sup>45</sup> erg]	Ref.	$E_{rad}$ <sup>b</sup> [10 <sup>45</sup> erg]	phy. sit.	$E_{rad}/E_{CO}$ <sup>c</sup>
Cep A	100	60	6.9	1	760	C-2	110
Cep A	9.3	87.5	10.0	2	71	C-2	7.1
Cep A	20	240	62	3	150	C-2	2.5
L1448	5.6	0.95	0.358	4	0.63	C-1	1.8
L1448					0.74	C-2	2.1
L1448					2.7	J-1	7.5
L1448					140	J-2	380

<sup>a</sup> The outflow age, momentum, and kinetic energy are measured by tracing high-velocity CO emissions.

<sup>b</sup> The radiative energy is calculated by assuming that the luminosity has been constant over the outflow age (Equation 5.15).

<sup>c</sup> The energy ratio ( $E_{rad}/E_{CO}$ ) is 1.5 for the energy conserving model, and 20 for the momentum conserving model.

References. — (1) Levreault 1988 (2) Choi, Evans, and Jaffe 1993 (3) Bally and Lada 1983 (4) Cabrit and Bertout 1992

## Chapter 6

### CONCLUSIONS

We have observed the  $\text{H}_2 v = 1 \rightarrow 0 S(1)$  ( $\lambda = 2.122\mu\text{m}$ ) transition line from shocked regions in the bipolar molecular outflows. In order to get the total shocked luminosity, we need to extrapolate from this line to the total cooling and we adopt the *C-type* shock model by Draine, Roberge, and Dalgarno (1983) and the *J-type* model by Hollenbach and McKee (1989). The simulation of the *C-type* shock model, however, cannot work at shock speeds over  $50 \text{ km s}^{-1}$ , because the  $\text{H}_2$  is fully dissociated and the physical situation at the shock front is dramatically changed. The *J-type* shock model, also, cannot explain the observed line ratios and the broadened spectral profiles.

We compare the observed radiation energy with the kinetic energy of the swept-up gas and we try to figure out that how efficiently the stellar wind transfers its kinetic energy to the ambient cloud. In the momentum conserving outflow model, the wind shock is totally radiative and the flow is isothermal. By contrast, the wind shock is not radiative and the flow is adiabatic in the energy conserving model. Note, however, that both of the models are extreme cases. The real outflow may have both of the features, which means that the energy ratios of  $E_{rad}/E_{CO}$  would be between 1.5 (energy conserving model) and 20 (momentum conserving model). This suggests that the statistical distribution of the energy ratios will have significant information on the outflow energetics.

Our detection of H<sub>2</sub> 2.122  $\mu$ m line in L1551 suggests further detailed 2.122  $\mu$ m observations of this object as well. L1551 is a promising outflow source in the energetics point of view, because the atomic hydrogen wind has been observed (Giovanardi et al. 1992) and the CO observations are very reliable (Moriarty-Schieven and Snell 1988). Tracing the weak and extended shocked intensity by 2.122  $\mu$ m will also discriminate the nature of the shock from the already observed Herbig-Haro objects.

## BIBLIOGRAPHY

- Bachiller, R., and Cernicharo, J. 1986, *A&A*, 168, 262
- Bachiller, R., Cernicharo, J., Martín-Pintado, J., Tafalla, M., and Lazareff, B.  
1990, *A&A*, 231, 174
- Bachiller, R., and Gómez-González, J. 1992, *ARA&A*, 3, 257
- Bally, J., and Lane, A. P. 1982, *ApJ*, 257, 612
- Bally, J., and Lada, C. J. 1983, *ApJ*, 265, 824
- Bally, J., and Lane, A. P. 1990, in *Astrophysics with Infrared Arrays*, ed. R.  
Elston (San Francisco: Book Crafters, Inc.), p.273
- Bally, J., Lada, E. A., and Lane, A. P. 1993, *ApJ* (BLL93)
- Beichman, C. A., Becklin, E. E., and Wynn-Williams, C. G. 1979, *ApJ*, 232,  
L47
- Blaauw, A., Hiltner, W. A., and Johnson, H. L. 1959, *ApJ*, 130, 69
- Born, M., and Wolf, E. 1965, *Principles of Optics* (Oxford: Pergamon Press)
- Cabrit, S., and Bertout, C. 1992, *A&A*, 261, 274
- Chapman, R., Beard, S. M., Mountain, C. M., Pettie, D. G., and Pickup,  
D. A. 1990, in *Instrumentation in Astronomy VII*, ed. D. L. Crawford  
(Washington: SPIE), p.34
- Choi, M., Evans II, N. J., and Jaffe, D. T. 1993, *ApJ*, 417, 624
- Dabrowski, I. 1984, *Can. J. Phys.*, 62, 1639
- Draine, B. T., Roberge, W. G., and Dalgarno, A. 1983, *ApJ*, 264, 485 (DRD83)
- Doyon, R., and Nadeau, D. 1988, *ApJ*, 334, 883 (DN88)

- Giovanardi, G., Lizano, S., Natta, A., Evans II, N. J., and Heiles, C. 1992, *ApJ*, 397, 214
- Hollenbach, D. J., Chernoff, D. F., and McKee, C. F. 1989, in 'Infrared Spectroscopy in Astronomy', *Proc. 22nd ESLAB Symposium*, ed. B. Kaldeich (Spain: ESA SP-290), p.245
- Hollenbach, D. J., and McKee, C. F. 1989, *ApJ*, 342, 306
- Horowitz, P., and Hill, W. 1989, *The Art of Electronics*, 2nd Ed. (USA: Cambridge University Press) p.180
- Kitchin, C. R. 1991, *Astrophysical Techniques* (New York: Adam Hilger) p.38
- Kwok, S., and Volk, K. 1985, *ApJ*, 299, 191
- Lane, A. P. 1989, in *Low Mass Star Formation and Pre-Main Sequence Objects*, ed. B. Reipurth (Garching: ESO), p.331
- Levreault, R. M. 1985, Ph.D. thesis, University of Texas at Austin
- Levreault, R. M. 1988, *ApJ*, 330, 897
- Lizano, S., Heiles, C., Rodríguez, L. F., Koo, B.-C., Shu, F. H., Hasegawa, T., and Hayashi, S. 1988, *ApJ*, 328, 763
- Luhman, M. L., Jaffe, D. T., Keller, L. D., and Pak, S. 1994, in preparation
- McKee, C. F., and Hollenbach, D. J. 1980, *ARA&A*, 18, 219
- McKee, C. F., and Hollenbach, D. J. 1987, *ApJ*, 322, 275
- McKee, C. F. 1989, *ApJ*, 345, 782
- Moore, J., Davis, C., and Coplan, M. 1988, *Building Scientific Apparatus* (USA: Addison Wesley), p.242
- Moriarty-Schieven, G. H., and Snell, R. L. 1988, *ApJ*, 332, 364
- Norman, C., and Silk, J. 1980, *ApJ*, 238, 158
- Rodríguez, L. F., Ho, P. T. P., and Moran, J. M. 1980, *ApJ*, 240, L149

- Scalo, J. M., and Pumphrey, W. A. 1982, *ApJ*, 258, L29
- Shu, F. H., Ruden, S. P., Lada, C. J., and Lizano, S. 1991, *ApJ*, 370, L31
- Snell, R. L., Loren, R. B., and Plambeck, R. L. 1980, *ApJ*, 239, L17
- Terebey, S. 1991, *Mem. S.A.It.*, 62, 823
- Torrelles, J. M., Verdes-Montenegro, L., and Ho, P. T. P. 1993, *ApJ*, 410, 202
- Turner, J., Kirby-Docken, K., and Dalgarno, A. 1977, *ApJS*, 35, 281
- Vincent, J. 1990, *Fundamentals of Infrared Detector Operation and Testing*  
(New York: Wiley-International Publication) p.56
- Yamashita, T., and Tamura, M. 1992, *ApJ*, 387, L93

## VITA

Soojong Pak was born in Seoul, South Korea, on April 7, 1967, the son of Kwang-Hyun Pak and Bok-Hee Lee. After graduating from Joong-Ang High School, Seoul, in 1986, he entered Seoul National University, Seoul, majoring in Astronomy. He received his degree of Bachelor of Science from Seoul National University in February, 1990. He re-entered a junior course in the Department of Electrical Engineering and studied for a year. In September, 1991, he entered the Graduate School of the University of Texas at Austin.

He married Soyoung Lee in June, 1991. She is also a graduate student in the program of Foreign Language Education in the University of Texas at Austin.

Permanent address: Kwang-Myung Villa F-3,  
Dongsoong-dong 129,  
Jongno-gu, Seoul 110-510,  
South Korea

This thesis was typeset <sup>1</sup>with L<sup>A</sup>T<sub>E</sub>X by the author.

---

<sup>1</sup>The L<sup>A</sup>T<sub>E</sub>X document preparation system was developed by Leslie Lamport as a special version of Donald Knuth's T<sub>E</sub>X program for computer typesetting. T<sub>E</sub>X is a trademark of the American Mathematical Society. The L<sup>A</sup>T<sub>E</sub>X macro package for The University of Texas at Austin thesis format was written by Khe-Sing The.